Bonding of hexagonal BN to transition metal surfaces: An *ab initio* density-functional theory study

Robert Laskowski, Peter Blaha, and Karlheinz Schwarz
Institute of Materials Chemistry, Technische Universität Wien, Getreidemarkt 9/165TC, A-1060 Vienna, Austria
(Received 16 April 2008; published 8 July 2008)

Hexagonal *h*-BN/metal interfaces for different 3*d*, 4*d*, and 5*d* metals are studied in terms of *ab initio* density functional theory. The trends across the periodic table of the bonding of *h*-BN to the metal surfaces are discussed. We show that the binding energy between *h*-BN and the metal surface decreases with the filling of the *d* shell and is largest for 4*d* elements. For all studied metals the N atom is repelled from the metal surface, whereas the B atom is attracted to it. The strength of attraction/repulsion of B and N atoms depends on their position relative to the underlying metal atoms, and only when N sits on-top of the metal and B occupies fcc or hcp hollow sites the B-attraction dominates the N repulsion and *h*-BN is bound to the surface. The structure of the *h*-BN/metal interface is a result of the balance between these forces and the lattice mismatch.

DOI: 10.1103/PhysRevB.78.045409 PACS number(s): 73.20.At, 73.22.−f

I. INTRODUCTION

Hexagonal boron nitride (*h*-BN) is known to bind to many transition metal surfaces forming a perfect hexagonal monolayer. The classical example of such an interface is *h*-BN/Ni(111), which forms by thermal decomposition of borazine $(HBNH)_6$ on a Ni(111) surface and was first reported by Nagashima and coworkers.[1] They investigated both valence-band and conduction-band structures using the angle-resolved ultraviolet photoelectron spectroscopy (ARUPS) and angle-resolved secondary emission spectroscopy. Furthermore, they did not find a substantial mixing of the Ni *d* states with *h*-BN π states indicating weak bonding between the metal surface and the monolayer. Subsequently, these authors[2] studied, in addition to Ni(111), also Pd(111) and Pt(111) surfaces. They showed, using ARUPS, that the electronic structure of a *h*-BN monolayer is almost independent of the substrate. However, they noticed that the bonding is stronger for Ni(111) than for the other two substrates. The same systems were studied by Rokuta and co-workers[3] with high-resolution electron energy loss spectroscopy. They concluded that some level of hybridization between Ni *d* and BN π states is present and is responsible for differences between the spectra measured for *h*-BN/Ni(111) and *h*-BN/Pt(111) or *h*-BN/Pd(111). Their low-energy electron diffraction (LEED) results indicate that *h*-BN is not completely flat but slightly buckled on Ni(111) with B being closer to the surface than N. This buckling was attributed to the small lattice mismatch between *h*-BN and Ni(111), which leads to a commensurate 1×1 system where *h*-BN is slightly compressed and thus buckles. The structural model was confirmed further by Auwärter *et al.*[4] with N-1*s* and B-1*s* x-ray photoelectron diffraction (XPD) and scanning tunneling microscopy (STM), and Muntwiler *et al.*[5] with x-ray photoelectron diffraction. The theoretical work based on density functional theory (DFT) by Grad *et al.*[6] reproduced the observed STM pictures and found that a stable *h*-BN monolayer only forms when N is on-top of Ni (with B either in the fcc or hcp hollow site) with a rather weakly bound character of the *h*-BN monolayer. Huda and Kleinman[7] showed that the calculated binding of *h*-BN to Ni(111) critically depends on the choice of the density functional used. They concluded that, only the local-density approximation (LDA) results in a bound state, whereas the generalized gradient approximation (GGA) gives a metastable bounded structure, which, however, is still close to the experimental one. Ni 3*d*-BN π hybridization was experimentally studied by Preobrajenski *et al.* with core-level spectroscopies.[8] They observed significant changes in some spectral features compared to bulk *h*-BN and they interpreted this as manifestation of a strong hybridization between Ni-*d* and BN-π states suggesting a rather strong interaction between *h*-BN and the metal surface. Further studies by these authors[9] using near-edge x-ray absorption fine-structure and photoemission spectroscopies supported these conclusions.

The successful formation of a *h*-BN monolayer has, besides for *h*-BN/Ni(111), also been reported for Cu(111) (Ref. 9), Pt(111) (Ref. 10), Pd(111) (Ref. 11), Pd(110) (Ref. 12), Rh(111) (Ref. 13), and Ru(001) (Ref. 14) surfaces. The *h*-BN/Cu(111) interface is a 1×1 commensurate structure such as the Ni(111) case. However its bonding is much weaker than in the *h*-BN/Ni(111) case.[9] The structure of all other interfaces mentioned above is affected by a considerable lattice mismatch between *h*-BN and the metal surface, which varies between 7% and 10% depending on the substrate. For *h*-BN/ Pt(111) (Ref. 10), Pd(111) (Ref. 11), and Pd(110) (Ref. 12) interfaces, STM images show some moiré patterns. However for Rh(111) (Ref. 13) and Ru(001) (Ref. 14) systems, a well ordered nanostructure with a periodicity of about 3 nm was observed. In this case a strong (about 1 eV) splitting of *h*-BN σ bands was measured with ultraviolet photoelectron spectroscopy (UPS). This was one reason why instead of a simple monolayer the formation of a more complicated structure (partial double-layer model) was suggested, which was called "BN-nanomesh."[13] However, theoretical investigations[15] of this interface showed that a highly corrugated monolayer of *h*-BN in a 12×13 commensurate geometry [a 13×13 supercell of *h*-BN on top of a 12×12 supercell of Rh(111)] exhibit a very similar σ-band splitting and it can also explain the observed STM images.[16] The structure is a result of a delicate balance between repulsive forces acting on N and attractive forces acting on the B at-

 ©2008 The American Physical Society

oms. Since the actual absolute values of these forces vary with the lateral BN position with respect to the Rh substrate surface in the supercell, the *h*-BN monolayer deforms vertically. This theoretical corrugated monolayer structure was confirmed by recent STM images by Berner *et al.*[17] From a structural point of view the differences between various substrates are thus rather quantitative than qualitative in nature. In all cases, except for the strictly 1×1 commensurate Ni(111) and Cu(111) systems, the *h*-BN monolayer shows a regular vertical deformation. The structure of this deformation depends on the symmetry of the substrate. For all hexagonal surfaces one observes a hexagonal superstructure whose size depends on the lattice mismatch between *h*-BN and the metal surface, whereas some kind of one-dimensional superstructures are formed as shown for the Pd(110) (Ref. 12), Mo (Ref. 18), and Ni(110) (Ref. 19) surfaces. Besides the lattice mismatch, the main difference between the mentioned *h*-BN/metal interfaces is of course the varying strength of interaction between *h*-BN and the metal surface. Despite the fact that the general structure remains very similar for all large lattice mismatch systems, the stronger bound interfaces as *h*-BN/Rh(111) and *h*-BN/Ru(001) are still referred in literature as "nanomesh." The formation of a nanomesh attracted much attention since it could be a possible substrate for molecular deposition by supporting self-assembling molecular structures.[17,20] Moreover this structure is found to be stable under ambient conditions and even in aqueous solutions, which would provide an important basis for technological applications such as templating and coating.[17,21,22]

As already mentioned, the properties of *h*-BN deposited on metal surfaces depends mainly on the strength of its interaction with the metal substrate. Therefore it is interesting to study this interaction with a broader perspective by inspecting the trends across the periodic table. In this work we present a series of theoretical studies of the *h*-BN-metal bonding, based on the *ab initio* approach in the framework of DFT, performed for several 3*d*, 4*d*, and 5*d* metal substrates. The paper is organized as follows: The next section describes the applied methodology. After that we discuss the bonding of the stable *h*-BN configuration and describe the trends in the bonding of *h*-BN to the metal surfaces. We also propose an explanation for the observed behavior. Furthermore, the effects of the lattice mismatch and the origin of the corrugation of the *h*-BN layer in the nanomesh unit cell are discussed.

II. METHOD

The *ab initio* calculations presented in this work have been performed with the WIEN2K code,[23] which uses the linear augmented plane wave plus local orbital method (LAPW+LO) (Ref. 24) and is based on DFT. We are interested here in the properties of the *h*-BN/metal interfaces. Depending on the structure of the substrate, the *h*-BN is deposited on the (111) surfaces for face-centered cubic (fcc) metals or the (001) surfaces for hexagonal-closed packed (hcp) metals. The surface calculations have been performed in slab geometry, involving seven metal layers for fcc metals and eight layers for hcp metals. For all calculations a commensurate 1×1 geometry has been applied. In each case the thickness of the vacuum region was set to about 10 Å. The Brillouin zone integration was done with a $14\times14\times1$ mesh. The LAPW+LO basis quality, measured by the product $R_{\min}K_{\max}$ ($R_{\min}$-minimal atomic sphere radius and $K_{\max}$-length of maximal reciprocal lattice vector), was set to 6.0. The atomic sphere radii for metal atoms were set to 2.25 a.u. and for B and N atoms to 1.35 a.u., except for the Co and Ni systems where the N and B radii had to be reduced to 1.3 a.u. All parameters have been tested against numerical convergence. The structures have been optimized until the atomic forces dropped below 1 mRy/a.u. For all results presented here the recent Wu-Cohen generalized gradient approximation (WC-GGA) has been used.[25] It has been shown[26] that this functional slightly improves the performance compared to the standard Perdew-Burke-Ernzerhof (PBE) (Ref. 27) GGA or the LDA when applied to metal surfaces. Only in Table I we show results calculated with the standard LDA and the PBE (Ref. 27) GGA in order to briefly discuss the effects due to choice of the applied functional.

TABLE I. Binding energies ΔE (eV/BN) and geometries (Å) of *h*-BN/transition metal systems: vertical metal (M)-N ($z_{\text{M-N}}$) and vertical B-N ($z_{\text{B-N}}$) distances. A negative value for ΔE indicates an unbound system. In all cases the B atom is closer than the N atom to the metal surface.

		LDA			PBE			WC		
		ΔE	$z_{\text{M-N}}$	$z_{\text{B-N}}$	ΔE	$z_{\text{M-N}}$	$z_{\text{B-N}}$	ΔE	$z_{\text{M-N}}$	$z_{\text{B-N}}$
3d	Co	0.32	2.14	0.11	0.06	2.14	0.12	0.23	2.15	0.12
	Ni	0.27	2.12	0.11	0.04	2.15	0.11	0.19	2.14	0.11
	Cu	0.19	3.10	0.02	−0.01			0.05	3.00	0.01
4d	Ru	0.98	2.13	0.14	0.64	2.18	0.15	0.85	2.17	0.15
	Rh	0.61	2.16	0.13	0.31	2.20	0.14	0.50	2.18	0.14
	Pd	0.47	2.21	0.11	0.20	2.25	0.12	0.36	2.25	0.12
	Ag	0.19	2.55	0.04	−0.01			0.10	2.78	0.03
	Ir	0.49	2.20	0.14	0.20	2.24	0.15	0.38	2.23	0.15
5d	Pt	0.34	2.26	0.12	0.05	2.31	0.13	0.19	2.30	0.13
	Au	0.16	2.95	0.02	−0.03			0.07	2.93	0.03

III. RESULTS AND DISCUSSION

A. Bonding configuration

Now there is a common agreement that for commensurate 1×1 geometries observed in *h*-BN/Ni(111) or *h*-BN/Cu(111) the N atoms reside on top of the surface metal atoms, whereas the B atoms are in the fcc hollow sites.[6] It is also known that, at least for the Ni case, the interface configuration, in which the B atom sits in the hcp position, is stable with a slightly higher total energy.[6] This nicely explains the experimentally observed domain structure with a 30° angle between different domains.[28] All other configurations would lead to unstable interfaces.[6] Here we focus on the (B fcc, N top) geometry only. In order to study the bonding properties systematically across the 3*d*, 4*d*, and 5*d* metals in this sec-

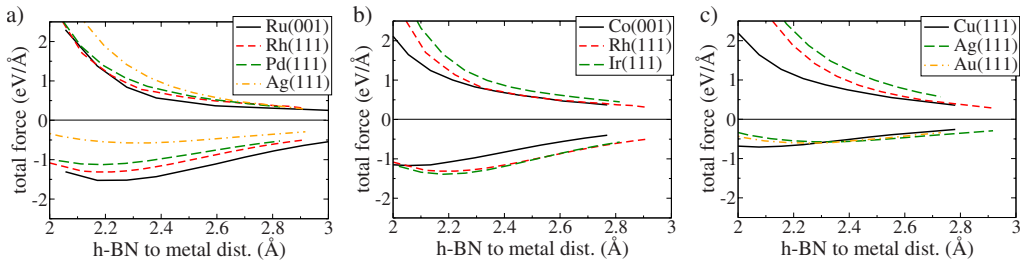

FIG. 1. (Color online) The forces acting on N (positive) and B (negative) calculated for a flat *h*-BN layer in (fcc, top) position. (a) Trends for interfaces with 4*d* metals. (b) Comparison of 3*d*, 4*d*, and 5*d* elements. (c) Interactions with noble metals

tion, we ignore consequences of the lattice mismatch and consider all interfaces to be commensurate the 1×1 systems. Of course, this implies a lot of strain on the BN layer. The effects of incommensurate lattice sizes will be discussed in the next section.

The effect of the applied functional on the binding energy of *h*-BN to the metal surfaces was discussed by Tran *et al.*[26] in connection with the WC-GGA functional. For clarity and completeness we also present these results here. Table I contains the binding energies of *h*-BN for a set of 3*d*, 4*d*, and 5*d* metal surfaces, as well as the basic structural parameters calculated with LDA, PBE, and WC functionals. The binding energies have been calculated by comparing the total energies of the *h*-BN/metal interfaces with pure metal surfaces and a free *h*-BN layer. In order to eliminate the effect of straining *h*-BN the energy of the free *h*-BN layer was calculated with the lattice parameters of the underlying metal surface. As evident from Table I, clear tendencies can be seen: for all elements, LDA yields the largest binding energies, while PBE-GGA gives the weakest bonding; in the case of noble metals the resulting interfaces are even unstable, which is, for Cu and possibly also Au, in contrast to the experimental facts.[9,29] The results obtained with the WC functional fall in between LDA and PBE. Although the absolute binding-energy values depend on the functional, the observed trends are rather insensitive to it. Across the 3*d*, 4*d*, and 5*d* rows of the periodic table the binding energy decreases from left to right. The calculated binding is biggest for the 4*d* elements and smallest for 3*d* series. A natural consequence of the changes in the binding strength is the change in some structural parameters of the commensurate *h*-BN layer. The distance between N atoms and the top metal atoms increases within each row of the periodic table, with a small exception for the magnetic Ni and Co systems. There is also a significant increase in the distance for noble metals, as the interaction is very weak in this case. For all substrates, except the noble metals, the *h*-BN layer is buckled by about 0.1 Å with the B atom closer to the metal surface. It was suggested by Rokuta *et al.*[3] that this buckling comes from the necessary contraction of the BN-bond distance in order to form a commensurate structure for the Ni and Co systems. We will demonstrate below that it is the interaction between N and B with the metal atoms at the interface, which leads to this buckling. In fact, for most cases the BN-distance needs to expand in order to match the metal substrate lattice but still a sizeable buckling occurs. We can understand this effect by putting a flat *h*-BN on top of the metal substrate at an average BN-metal distance in the (B fcc, N top) geometry. The calculated forces (Fig. 1) acting on B and N atoms, respectively, indicate a repulsion (positive forces) of the N atoms from the surface but an attraction of the B atoms toward the surface (negative force). The forces on N vary much stronger with distance from the metal surface than the B force. Moreover the N force decreases exponentially with distance, while the force acting on B shows a clear maximum of its absolute value. The actual equilibrium positions and the resulting buckling is clearly a balance between the attraction and repulsion of B and N atoms and the strong σ and π bonds between B and N, which try to keep *h*-BN flat. The value of the buckling naturally decreases with the distance from the surface, since the forces acting on N and B decrease with a larger distance from the metal.[15] The buckling is also larger for strongly bound *h*-BN and smaller for weakly bound layers, thus it is almost disappearing for noble metals. According to the experimental estimates of the structural parameters of *h*-BN/Ni(111) given by Rokuta *et al.*,[3,4] the N-metal distance is close to 2.2 Å and the buckling is around 0.1 Å. These values are very close to the PBE and WC results, while LDA clearly overbinds *h*-BN to the Ni surface.

A clear trend is observed for the *h*-BN binding energies across the periodic table and the observed forces follow this trend. For example, the results for the 4*d* row are shown in Fig. 1(a). For the Ru(001) surface, where the binding energy of *h*-BN (see Table I) has the largest value, the attracting force on B is the biggest among all 4*d* elements, while the repulsion of N has the smallest value. On the other side of the periodic table, for Ag(111) where *h*-BN is only weakly or not bounded at all, the B attraction is weakest and the N repulsion is the strongest. The trends within a column in the periodic table are displayed in Figs. 1(b) and 1(c). For the Co(001), Rh(111), and Ir(111) sequence, the Co(001) surface has the weakest bonding and consequently the smallest B attraction. Rh(111) and Ir(111) have similar B attractions, however, the N atom is less repelled on Rh(111) than on Ir(111), which is fully compatible with the results from Table I. An interesting behavior can be seen in the sequence of the noble metals [Fig. 1(c)] where the B attraction is almost unchanged, whereas the N repulsion strongly varies between the elements.

The trends presented above can be correlated with the electronic structure of the interfaces. The *h*-BN to metal bonding is mainly driven by hybridization of N-p_z and B-p_z with metal-d_{z^2} orbitals. The corresponding partial density of states (DOS) of the interfaces and the clean metal surfaces

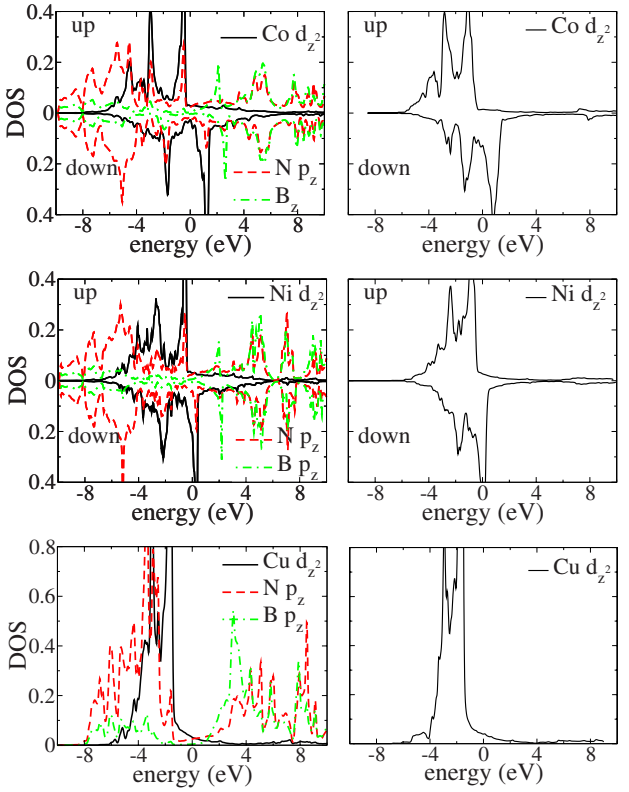

FIG. 2. (Color online) Calculated projected density of states of surface Me-d_{z^2}, B-p_z ($\times 3$), and N-p_z ($\times 3$) states for 3d metal/BN interfaces (left column). Calculated projected density of states of surface Me-d_{z^2} states for clean 3d metal surfaces (right column)

for 3d, 4d, and 5d elements are presented in Figs. 2–4, respectively, while the p_z DOS of a free monolayer of h-BN is shown in Fig. 5. For the latter case the free h-BN monolayer shows a characteristic bonding-antibonding splitting into π and π^* states with a gap of more than 4 eV. The largest peaks of the DOS are located right around the gap with some tail-like structures into low/high-energy regions below/above the gap, respectively. As expected from electronegativity and atomic numbers, the occupied π states have predominantly N character, while in the unoccupied π^* states the B contribution dominates. The free metal surfaces show also quite characteristic structures in the DOS, such as a fairly broad three-peak structure (spin splitted for Co and Ni) for the non-noble metals but a rather narrow two-peak structure for the noble metals. The number of d-electrons determines the position of these bands with respect to Fermi energy (E_F). For the noble metals the d_{z^2} DOS is well below E_F, whereas for earlier TM the highest peak in the DOS is almost completely unoccupied. Related to the 3d, 4d, or 5d character of the corresponding wave functions, the DOS is quite narrow for 3d elements but fairly broad for 5d metals. However in all cases there is a fairly sharp drop of the DOS after the last dominant peak. Comparing the DOS of the BN/metal interfaces (left panel) with the free surfaces (right panel), it is evident that the strength of the h-BN-metal bonding is also reflected in the changes in the DOS. For the noble metals the DOS of the interfaces is composed of an almost unmodified DOS of the isolated metal surface, and also the B and N DOS keep there

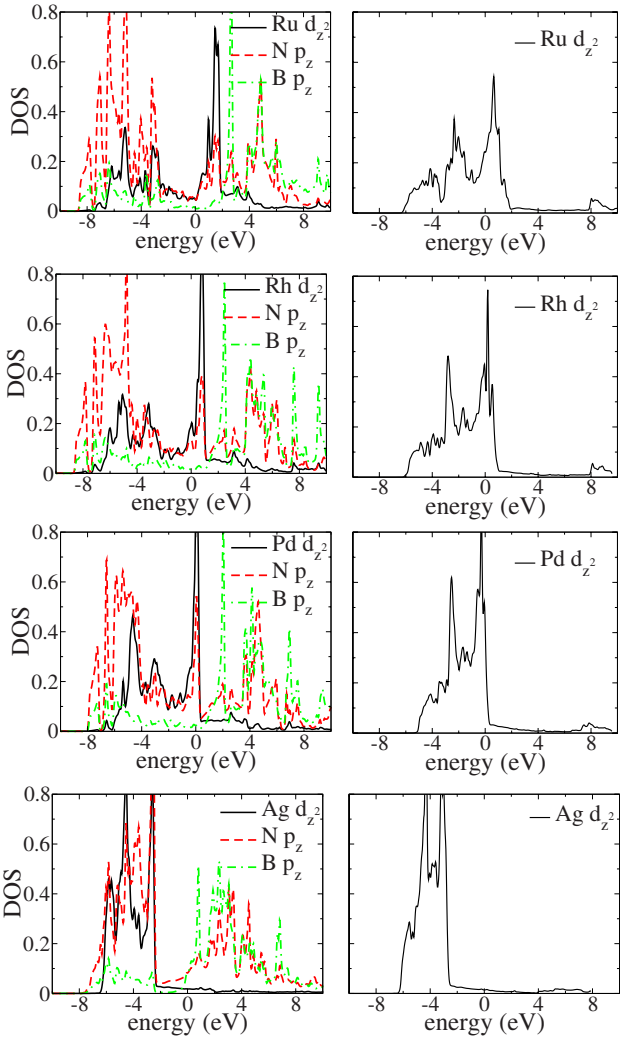

FIG. 3. (Color online) Calculated projected density of states of Me-d_{z^2}, B-p_z ($\times 3$), and N-p_z ($\times 3$) states for 4d metal/BN interfaces (left column). Calculated projected density of states of Me-d_{z^2} states for clean 4d metal surfaces (right column)

characteristic gapped structure. On the other hand for the cases where h-BN strongly binds to the substrate [Ru(001) or Rh(111)], the modification of the DOS is rather substantial. The metal d_{z^2} DOS in the interface is significantly wider than for the free surface with much of the weight shifted from lower-energy and higher-energy regions characteristics to a bonding-antibonding interaction. For all nonmagnetic interfaces, except the noble metals, the d_{z^2} DOS is composed of three well separated peaks, on average at around -5, -3, and 0 eV. The distance between the first two peaks decreases slightly for weakly bound cases and vanishes suddenly for noble metals. The position of the third peak depends strongly on the substrate and it mainly resembles the changes in the DOS of the free metal surfaces. For strongly bound interfaces it is well above the Fermi level, and for noble metals well below it. In addition, there are small but important contributions at even higher energies (not present at all in the free surfaces) for the strongly interacting cases, which originate from a strong antibonding interaction with B-p_z and N-p_z states (see the peaks at 3 and 4 eV for Ru and Rh

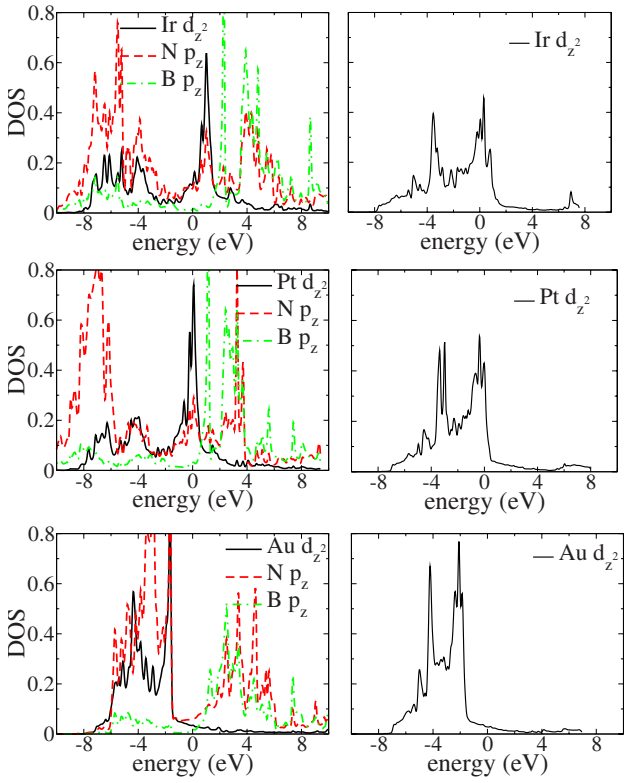

FIG. 4. (Color online) Calculated projected density of states of Me-d_{z^2}, B-p_z (×3), and N-p_z (×3) states for 5*d* metal/BN interfaces (left column). Calculated projected density of states of Me-d_{z^2} states for clean 5*d* metal surfaces (right column)

interfaces). In the strongly interacting cases, the influence on the N-p_z and B-P_z states is of course also substantial. The B and N DOS gets broader and, in particular, the weight of N-p_z states is shifted to lower energies. The characteristic gap of about 4 eV in free *h*-BN vanishes for the interfaces and gets filled (again mainly due to N-p_z states) and additional peaks appear also in the unoccupied part of the DOS, which is responsible for the observed "prepeak" features in near-edge x-ray-absorption fine-structure (NEXAFS) spectra.[10,30] In summary, a strong hybridization pattern with

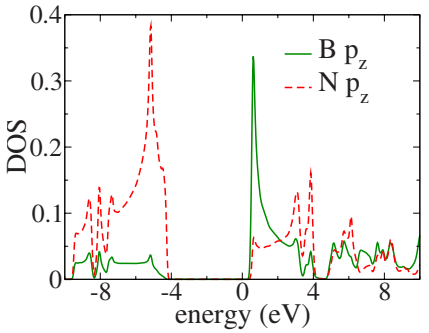

FIG. 5. (Color online) Calculated projected density of states of B-p_z and N-p_z states for a monolayer of *h*-BN.

bonding-antibonding interactions of metal d_{z^2} and N p_z states is observed for all cases except for the noble metals. The third (highest) metal d_{z^2} peak overlaps with a N-p_z peak.

In order to quantify the correlation between changes in the electronic structure and the strength of the *h*-BN-metal bonding, we calculate the partial charges inside atomic spheres corresponding to metal-d_{z^2} and N and B-p_z character. These quantities correspond to the integrals of the respective partial DOS (Figs. 2–5) up to the Fermi level. Table II summarizes the values calculated for all interfaces as well as for the free metal surfaces and the free *h*-BN monolayer. The effect of the interaction is related to the difference of these values, which are shown in the bottom panel of Table II. ΔB-p_z strictly correlates with the interaction strength. For all 3*d*, 4*d*, and 5*d* series the ΔB-p_z value is maximal for the most strongly bound interface but close to zero for noble metals. For ΔN-p_z, however, this correlation is not strictly fulfilled because ΔN-p_z is maximal for Rh(111) and Pt(111) surfaces, which have a slightly lower binding energy than Ru(001) or Ir(111), respectively (see Table I). In any case, both partial charges increase when the interface has been formed indicating an increased p_z occupation. The *h*-BN-metal interaction significantly affects also the Me-d_{z^2} charge of the top-layer metal atoms with a correlation similar to ΔN-p_z but an opposite sign. For all interfaces the Me d_{z^2} charge decreases compared to the free surfaces. It is worth noting that similar differences calculated for the total charges

TABLE II. Partial charges inside atomic spheres (in e^-) of d_{z^2}-top metal layer, p_z-N, and B character. First panel is for the interfaces, second panel for the free metal surfaces and free *h*-BN layer (with the lattice size matching the size of the corresponding metal surface), and third panel lists the differences between them.

	3*d*			4*d*				5*d*		
	Co	Ni	Cu	Ru	Rh	Pd	Ag	Ir	Pt	Au
Int., Me d_{z^2}	1.340	1.475	1.842	0.915	1.073	1.375	1.747	0.962	1.227	1.627
Int., N p_z	0.779	0.780	0.716	0.746	0.758	0.735	0.708	0.746	0.793	0.708
Int., B p_z	0.144	0.140	0.126	0.159	0.151	0.133	0.105	0.147	0.141	0.101
Met. surf., Me d_{z^2}	1.381	1.616	1.838	1.040	1.298	1.555	1.746	1.168	1.415	1.622
h-BN, N p_z	0.683	0.683	0.722	0.718	0.719	0.718	0.718	0.718	0.718	0.718
h-BN, B p_z	0.123	0.123	0.129	0.114	0.116	0.112	0.105	0.114	0.110	0.104
Δ Me d_{z^2}	−0.041	−0.141	0.004	−0.125	−0.225	−0.180	0.001	−0.206	−0.188	0.005
Δ N p_z	0.096	0.097	−0.006	0.028	0.039	0.017	−0.010	0.028	0.075	−0.010
Δ B p_z	0.021	0.017	−0.003	0.045	0.035	0.021	0.000	0.033	0.031	−0.003

TABLE III. The total charges inside atomic spheres (in e^-) of the top-layer metal atom, N and B. The upper panel shows the values for the interfaces, the middle panel for free metal surface and *h*-BN (with the lattice size matching the size of the corresponding metal surface), and the bottom panel gives the differences between them.

		3*d*			4*d*				5*d*	
	Co	Ni	Cu	Ru	Rh	Pd	Ag	Ir	Pt	Au
Me	26.051	27.102	27.929	41.906	43.066	44.143	45.099	74.513	75.562	76.565
N	5.153	5.151	5.291	5.152	5.169	5.120	5.039	5.145	5.100	5.025
B	3.061	3.063	3.101	2.951	2.970	2.914	2.833	2.939	2.890	2.818
Met. surf,Me	25.901	26.962	27.851	41.816	42.968	44.077	45.089	74.404	75.491	76.551
h-BN, N	5.153	5.153	5.290	5.139	5.162	5.115	5.039	5.135	5.094	5.026
h-BN, B	3.058	3.059	3.104	2.935	2.959	2.910	2.835	2.931	2.889	2.823
Δ Me	0.150	0.140	0.078	0.090	0.098	0.066	0.010	0.109	0.071	0.014
Δ N	0.000	−0.002	0.001	0.013	0.007	0.005	0.000	0.010	0.006	−0.001
Δ B	0.003	0.004	−0.003	0.016	0.011	0.004	−0.002	0.008	0.001	−0.005

inside the atomic spheres show much weaker dependences on the substrate (see Table III). This indicates a charge flow from N-p_{xy} and B-p_{xy} states to N-p_z and B-p_z, and from metal-d_{z^2} to the rest of the *d* orbitals. It is also interesting to note that the difference of the total charges calculated for the metal atoms (Table III, ΔMe) indicates a strong charge transfer (CT) toward the metal (opposite to the differences in the Me d_{z^2} charges). A corresponding negative CT for B and N cannot be observed since their charges are much more delocalized and are outside of the corresponding atomic spheres.

We have done a similar analysis based on charges calculated within Bader's "atoms in molecules" (AIM) method.[31] In this method an atom (atomic basin) is defined by the surface where the flux $\nabla\rho(r)\times\vec{n}=0$ is zero. The electron density is integrated within this boundary defining an atomic charge. These AIM charges sum up to the sum of the nuclear charges in the unit cell (unless there is a non-nuclear maximum[32] in the electron density) and contain information on two effects: (i) a "topology" effect, i.e., already a superposition of neutral atomic densities located at the crystalline sites may lead to a significant "CT." (ii) a "real" CT due to the change in the electron density in the solid originating from chemical bonding, i.e., after the self-consistent-field (SCF) calculation have converged. We have tried to separate these effects and use a superposition of atomic densities as reference to get rid of the topology effect. For instance the superposition of atomic B and N densities for a free *h*-BN monolayer leads to a CT of 2.2 e^- from B to N, while the SCF cycle introduces a charge flow of about 0.65 e^- from B to N, which we judge as a reasonable value for the actual CT in *h*-BN. Unfortunately, even this definition suffers from the ambiguity in the definition of an "atomic" charge density. In particular for transition metal atoms a possible intraatomic *s*-*d* transfer can interfere with this separation of topology and CT effects.

In Table IV we show the differences of the AIM charges between SCF and superposed atomic densities for the interfaces and the free surfaces as well as their differences. For the free *h*-BN monolayer a CT of 0.65 e^- from B to N is evident at the BN equilibrium distance (3*d* metals), which increases significantly for larger distances (4*d* and 5*d* elements) leading to a more ionic character of strained BN. The CT for the surface atoms of the free metal surfaces is much smaller (about 0.02–0.05 e^-) and may indicate s-*d* transfer and topology effects, if we assume that for a metallic surface

TABLE IV. The differences between SCF AIM charges and superposed atomic AIM charges for interface (upper panel), pure metal slab, and *h*-BN with the lattice size matching the size of the corresponding metal surface (middle) panel. The difference between upper and middle panels are shown in lower panel.

		3*d*			4*d*				5*d*	
	Co	Ni	Cu	Ru	Rh	Pd	Ag	Ir	Pt	Au
Me	−0.090	−0.073	−0.046	−0.016	−0.027	−0.022	−0.032	−0.065	−0.026	−0.041
N	−0.496	−0.515	−0.661	−0.762	−0.733	−0.843	−1.055	−0.770	−0.884	−1.059
B	0.569	0.572	0.681	0.762	0.749	0.866	1.068	0.801	0.902	1.073
Met. surf,Me	−0.022	−0.026	−0.023	−0.052	−0.041	−0.027	−0.020	−0.055	−0.042	−0.031
h-BN, N	−0.596	−0.637	−0.712	−0.925	−0.925	−0.962	−1.073	−0.931	−1.003	−1.083
h-BN, B	0.596	0.637	0.712	0.925	0.925	0.962	1.073	0.931	1.003	1.083
Δ Me	−0.068	−0.047	−0.023	0.036	0.014	0.005	−0.012	−0.010	0.016	−0.010
Δ N	0.100	0.122	0.051	0.163	0.192	0.119	0.018	0.161	0.119	0.024
Δ B	−0.027	−0.065	−0.031	−0.163	−0.176	−0.096	−0.005	−0.130	−0.101	−0.010

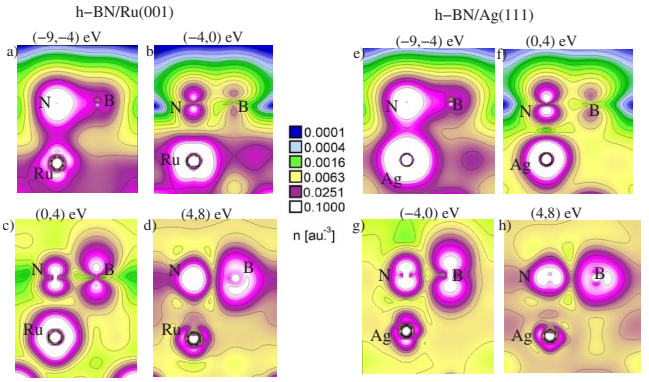

FIG. 6. (Color online) Charge-density distribution for *h*-BN/Ru(001) and *h*-BN/Ag(111) calculated for eigenstates from four energy regions with respect to the Fermi level: (a) and (e) from (−9,−4); (b) and (f) (−4,0); (c) and (g) (0,4) ; and (d) and (h) (4,8) eV

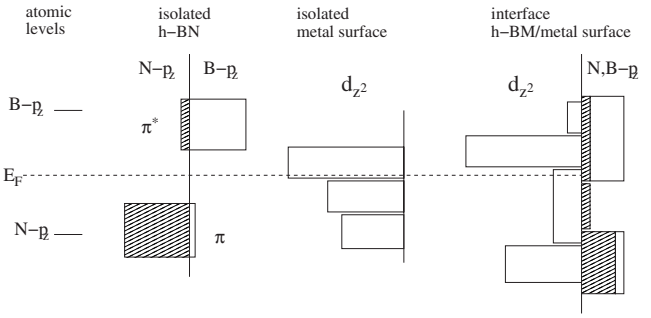

FIG. 7. Schematic diagram of the B-$_z$ and N-p_z (hatched areas) and the metal-d_{z^2} projected DOS for isolated *h*-BN, clean metal surface, and *h*-BN/Me interface.

all atoms should still be neutral. When the *h*-BN/metal interface is formed, we observe a CT $(\Delta N, \Delta B)$ back from N to B (strongest for the 4*d* series and weakest for 3*d* metals). For the 3*d* interfaces there is also an increased charge for the surface metal atom (reducing a magnetic moment of Ni by 0.06 μ_b) (Ref. 6), while the 4*d* elements show an opposite effect.

The interaction between *h*-BN and the metal surface can at first be understood just on a simple electrostatic basis. As we have seen in Table III, there is a CT to the top layer metal atom, and thus, the surface metal atom is negatively charged. Furthermore, it is evident that B is positively and N is negatively charged when BN is formed. Therefore, the negative N ion is repelled from the surface, but the positive B ion is attracted to the surface.

We have shown above that the *h*-BN-metal interaction is strongly related to the CT between N, B, and the metal atoms. The key player in the bonding mechanism is definitely the B atom since the changes on this element always correlate with the interaction strength. However, besides this simple electrostatic contribution, there are also strong covalent interactions, which are responsible for the changes in the partial DOS as discussed above. In order to demonstrate the various interactions more directly, we calculated the electron density from states in several energy windows above and below the Fermi energy separately. Figure 6 presents such densities calculated for *h*-BN/Ru(001) and *h*-BN/Ag(111) in energy windows with respect to Fermi level of (−9,−4), (−4,0), (0,4), and (4,8) eV (see Fig. 2–4 for the corresponding DOS of these energy ranges). In the first energy window (−9,−4) eV [Figs. 6(a) and 6(e)) the strong contribution from the σ *h*-BN bands (N-$p_{x,y}$ and B-$p_{x,y}$ states) is evident and leads to a large density between B and N. This, however, is of less importance for our discussion because there is not much change compared to a free BN monolayer. Much more important is the signature of strong bonding between the metal-d_{z^2}–N-p_z in this energy region. In the second (−4,0) eV [Figs. 6(b) and 6(f)] and third (0, 4) eV [Figs. 6(c) and 6(g)] energy windows there are not much BN-σ states present, but the π and π^* states dominate with a large N-p_z character in the lower-energy window but a large B-p_z character in the higher one in agreement with the partial DOS shown, e.g., in Fig. 5. Again more important for our discussion is the strong antibonding character between N-p_z and metal-d_{z^2} states [see, e.g., Figs. 6(b) and 6(f)]. It is evidenced by the low electron density between N and the metal, which indicates a node in the corresponding wave functions. Note that part of this antibonding interaction is visible already for states below E_F, i.e., these antibonding N-metal hybrids are partly occupied, and thus, explain why N is always repelled from the surface. On the other hand, when the N-metal interaction is antibonding in the π^* bands, the corresponding B-metal interaction must be bonding, a fact that explains why B is attracted to the surface [see, e.g., Fig. 6(c)]. The fourth energy window, (4, 8) eV above E_F [Figs. 6(d) and 6(h)], corresponds mainly to antibonding *h*-BN π and σ states with a fairly low metal contribution. A pronounced difference between *h*-BN/Ru(001) and *h*-BN/Ag(111) concerns, of course, the metal atoms. In agreement with the presented DOS the electron density of Ag is predominantly present in the first and second energy windows, since the *d* band is fully occupied and shifted below the Fermi level, while for Ru also some *d* states above E_F are present. Other differences (seen mainly in the second energy region) are the even lower density between N and the surface Ag atom, which indicates a much stronger antibonding situation for the N–metal interaction in *h*-BN/Ag(111) than in *h*-BN/Ru(001) and the weaker bonding features between B and Ag. For *h*-BN/Ru(001) the B charge is much more directed toward the metal layer [Fig. 6(b)], whereas for *h*-BN/Ag(111) it is rather localized on the B site. The observed differences fit nicely to the results presented in Fig. 1(a) where the N force increases but the magnitude of the B force decreases when the substrate is changed from Ru to Ag.

A schematic diagram of the B-p_z, N-p_z, and metal-d_{z^2} projected DOS is presented in Fig. 7. Since the atomic N-p_z level is much lower than B-p_z, the occupied part of the DOS for isolated *h*-BN, the BN π band, is mostly of N-p_z character, while the antibonding $\pi^\star$ band is dominated by B. The metal-d_{z^2} states are rather localized and their occupation (position with respect to E_F) depends on the electron number of the corresponding metal. When BN interacts with the metal-d_{z^2} states, an additional bonding-antibonding interac-

tion occurs and the DOS of the metal is enhanced and broadened in the low-energy region, while the hybridization of the antibonding BN hybrid ($\pi^\star$) (which is well above the Fermi level), broadens and enhances also the high-energy part of the metal DOS. This explains the observed electron transfer from the metal-d_{z^2} orbital to other d orbitals (which are not so much modified by the BN-metal interaction) and to N and B-p_z (Table II). Furthermore, the relatively strong hybridization between N and B with the metal atoms destroys the strict $\pi-\pi^\star$ splitting and N-p_z (and to a lesser degree B-p_z) states, which fill the h-BN band gap. This scenario was also supported by the electron-density plots shown above (Fig. 6) where the chemical bonds between N metal and B metal are clearly visible.

The important conclusion drawn from this analysis is that for N all bonding, nonbonding, but also a large part of the antibonding p_z-d_{z^2} states, are below the Fermi level. The amount of occupied antibonding states and thus the strength of the metal-N repulsion depends on the electron count of the metal. Elements with a more completely filled d-shell yield a much larger occupation of these antibonding states and thus result in a much stronger N repulsion. For the electropositive B the situation is different. The covalent interaction between B-p_z and d_{z^2} leads again to a large splitting into bonding and antibonding states with the metal. However, since the B-states are much higher in energy, more bonding states will be occupied while all antibonding states are even further pushed well above the Fermi level and thus are not occupied. This explains why B atoms are attracted to the surface, whereas N atoms are repelled from it.

B. Effect of lattice mismatch

The interaction of h-BN with metal surfaces is much weaker than the strong σ bonds between N and B. Therefore, an epitaxial growth of h-BN is only possible when the lattice sizes of the metal surfaces match approximately the lattice of free h-BN. This condition is only fulfilled for Co, Ni, and Cu (Fig. 8). For other metals discussed here the mismatch is rather substantial and straining h-BN would cost about 0.5 eV for Rh and Ru but even 2.0 eV for Ag and Au. This is comparable or even larger than the corresponding binding energies (see Table I). For these cases with a large lattice mismatch h-BN keeps its lattice parameter and the so-called nanomesh structures form. The resulting interface becomes periodic on a much larger length scale, which is determined by the matching condition $n_{\mathrm{BN}} \times a_{\mathrm{BN}} = n_{\mathrm{met}} \times a_{\mathrm{met}}$, where n_{BN} and n_{met} are the number of unit-cell repetitions of h-BN and the metal substrate, while a_{BN} and a_{met} are the corresponding lattice parameters. This condition is fulfilled with $n_{\mathrm{BN}}=13$ and $n_{\mathrm{met}}=12$ for Ru (Ref. 14) and Rh (Refs. 15 and 17), and for Pt (Ref. 10) with $n_{\mathrm{BN}}=10$ and $n_{\mathrm{met}}=9$. Therefore, within the nanomesh unit cell each B and N atom has a different neighborhood with respect to the metal substrate. The situation discussed in the previous section describes only the part of the nanomesh unit cell where the BN unit is close to the (B fcc, N top) or (B hcp, N top) position and the h-BN–metal bonding is realized as described above. Now we will concentrate on the part of the nanomesh unit cell where the BN unit

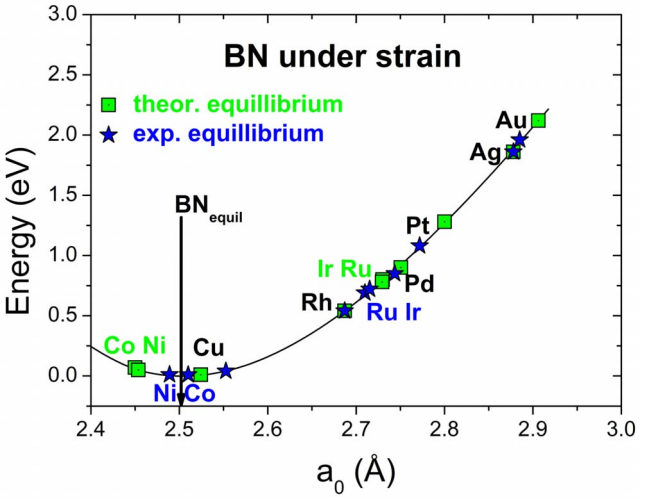

FIG. 8. (Color online) Energy vs a lattice parameter of bulk h-BN. The experimental and theoretical (WC-GGA) hexagonal lattice parameter ($a_{\mathrm{cub}} * \sqrt{2}$) of selected transition metals are also displayed.

is located at nonbonding positions, for example at (B top, N fcc) or (B fcc, N hcp) positions.

Figure 9 shows the forces acting on N and B atoms of a flat h-BN monolayer as a function of the distance from the Ru substrate for several high-symmetry arrangements of the h-BN layer. Since the situation for Rh and Pt is very similar to the Ru case, the following discussion is also valid for them. As we can see from Fig. 9 the (B fcc, N top) and (B hcp, N top) positions are the only cases where the B attraction exceeds the N repulsion. For all other configurations the B attraction is smaller than the N repulsion. The curves shown in Fig. 9 clearly separate into pairs. When the N or B atom is in the top position the forces do not depend much on the position of the other atom. We can see this for the two stable configurations with N top as well as for the two unstable configuration with B top. Similarly, the (B fcc, N hcp) and (B hcp, N fcc) configurations result in N and B forces, which are relatively close.

In order to explain the above observations we first look at the charge density of h-BN/Ru(001) (Fig. 10) stemming from

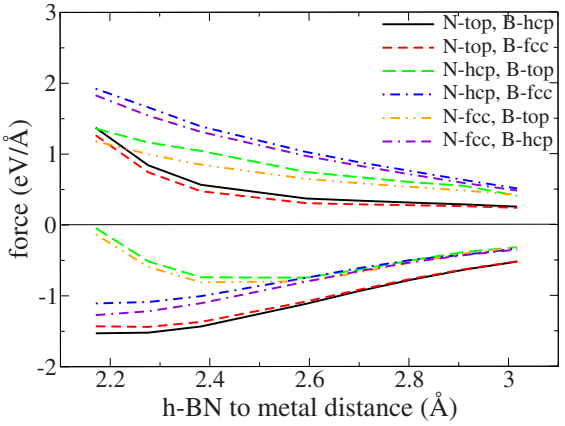

FIG. 9. (Color online) Forces acting on N (positive) and B (negative) calculated for a flat h-BN monolayer in different configurations of h-BN/Ru(001).

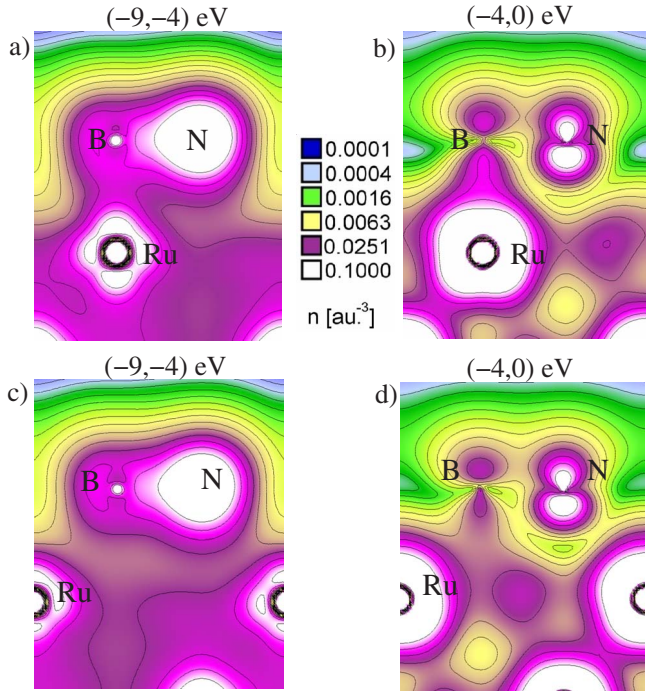

FIG. 10. (Color online) Charge-density distribution for *h*-BN/Ru(001) in nonbonding configurations (BN-Ru distance of 2.1 Å) calculated from states in energy window (−9,−4) eV for (a) and (c) and window (−4,0) eV for (b) and (d) with respect to Fermi level. For (a) and (b) *h*-BN is in (B top and N fcc) position and for (c) and (d) in (B fcc, N hcp).

states of two different energy regions below the Fermi level, (−9,−4) and (−4,0) eV, and from two different configurations, (B top, N fcc) and (B fcc, N hcp). These densities should be compared with those in the (B fcc, N top) configuration [Figs. 6(a) and 6(b)] already discussed above. For the energy window (−9,−4)eV the densities show mainly the B-N-σ bonds with some (smaller) covalent metal character. The states above −4 eV are much strongly affected by the change in the *h*-BN configuration. The B atom shows bonding character to Ru and in the B-top configuration the hybridization is much stronger than in B fcc, but in any case the B-p_z contribution is relatively small compared to the N-top configurations. The N atom for non-N-top positions shows strong asymmetry due to an *s*-*p* hybridization. Moreover the charge-density maxima appear in the diagonal direction between N-Ru manifesting antibonding interactions with $d_{yz,xz}$ orbitals. Interestingly the B atom in these positions shows direct vertical bonds to the metal surface. The reason for this different behavior is a difference in the spatial range of the 2*p* radial functions of N and B. As the N-*p* orbital is much lower in energy than B-*p*, it is much more localized than B-*p*. In the nontop position the distance to the metal atoms increases, therefore in order to interact with metal *d* orbitals the N-*p* states hybridize with N-*s* states. This is less favorable than direct interactions in the N-top position and results in stronger repulsion of the N atom. The B-*p* function is more diffuse, so the s-*p* mixing is not necessary, however in the B-top configuration the equilibrium distance between B and metal surface is much larger than in the nontop positions.

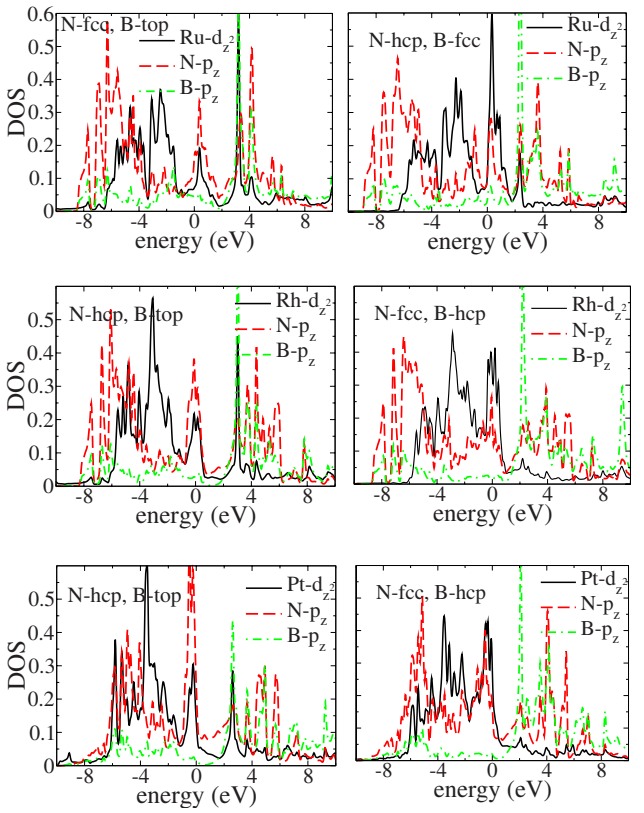

FIG. 11. (Color online) Calculated projected density of states of Me-d_z^2, B-p_z (×3), and N-p_z (×3) for Ru, Rh, and Pt interfaces with *h*-BN in nonbonding positions.

The differences in the *p*-*d* interaction are reflected in the DOS. Figure 11 collects N-p_z, B-p_z, and metal-d_{z^2} partial DOS for Ru, Rh, and Pt in two nonbonded configurations. For the B-top nonbonding configurations the metal states do not show a shift of d_{z^2} weight to lower energies and only above E_F the strong interaction with B is visible. The π^* bands above the Fermi level are spitted into a sharp peak below 4 eV, which comes from the interaction with B-p_z while the peak from the N-*p* interaction is pinned at the Fermi level. This pushes more of the N-*p* antibonding states below the Fermi level. The reduced bonding effect is even stronger for nontop configurations, where the metal-*d* DOS closely resembles the DOS calculated for free metal surfaces.

IV. CONCLUSIONS

In this work we have presented a DFT study of the *h*-BN/metal interface for a large set of 3*d*, 4*d*, and 5*d* metals surfaces, with the main emphasis on the *h*-BN-metal binding. For all metals the N atom is repelled from the metal surface, whereas the B atom is attracted to it. The structure of the *h*-BN layer is a results of a balance between these forces. This concerns both commensurate interfaces such as *h*-BN/Ni(111) or *h*-BN/Cu(111) and nanomesh (incommensurate) structures such as *h*-BN/Ru(001) or *h*-BN/Rh(111). The results for (B fcc or B hcp, N top) configurations indicate a clear trend in the strength of the binding energy between *h*-BN and the metal surface. This binding decreases

with the filling of the *d* shell and reaches its maximum for 4*d* elements. In a simple picture the interaction between *h*-BN and the metal surface can be understood just on an electrostatic basis. There is a small CT to the surface metal atoms and therefore the negative N ion is repelled from the surface while the positive B is attracted to it. The explanation of the observed trends across the periodic table, however, needs to analyze the covalent interactions between N and B-*p* states with the metal-*d* states. As we have shown, the N-*p* states are located near the bottom of the *d* band, whereas the B-*p* states are mainly above the Fermi level. Therefore the BN π band is dominated by N-*p* states, while the $\pi^\star$ band has a stronger contribution from B-*p* states. When the π bands interact with metal-*d* states they do not result in additional binding since both the bonding and antibonding part of this interaction are below E_F and thus are occupied. However, the interaction with the $\pi^\star$ band pushes some B-*p*-metal bonding and N-*p*-metal antibonding states (in the $\pi^\star$ band the phases of B-*p* and N-*p* are opposite) below the Fermi level. This results in the B attraction and the N repulsion. In order to bring some insight into the origin of the corrugation in nanomesh structures we discussed also *h*-BN in nonstable configurations. We showed that in these cases the B attraction decreases and the N repulsion increases with respect to the stable N-top configuration. The reason for this is related to the different spatial range of the N-*p* and B-*p* orbitals.

ACKNOWLEDGMENTS

This work was supported by the EU (Grant No. FP6-013817), the Austrian Research Fund (Grant No. SFB Aurora F1108), and the Austrian Grid Project (Grant No. WP-A15).

[1] A. Nagashima, N. Tejima, Y. Gamou, T. Kawai, and C. Oshima, Phys. Rev. B **51**, 4606 (1995).
[2] A. Nagashima, N. Tejima, Y. Gamou, T. Kawai, and C. Oshima, Phys. Rev. Lett. **75**, 3918 (1995).
[3] E. Rokuta, Y. Hasegawa, K. Suzuki, Y. Gamou, C. Oshima, and A. Nagashima, Phys. Rev. Lett. **79**, 4609 (1997).
[4] W. Auwärter, T. J. Kreutz, T. Greber, and J. Osterwalder, Surf. Sci. **429**, 229 (1999).
[5] M. Muntwiler, W. Auwärter, F. Baumberger, M. Hoesch, T. Greber, and J. Osterwalder, Surf. Sci. **472**, 125 (2001).
[6] G. B. Grad, P. Blaha, K. Schwarz, W. Auwärter, and T. Greber, Phys. Rev. B **68**, 085404 (2003).
[7] M. N. Huda and L. Kleinman, Phys. Rev. B **74**, 075418 (2006).
[8] A. B. Preobrajenski, A. S. Vinogradov, and N. Mårtensson, Phys. Rev. B **70**, 165404 (2004).
[9] A. B. Preobrajenski, A. S. Vinogradov, and N. Mårtensson, Surf. Sci. **582**, 21 (2005).
[10] A. B. Preobrajenski, A. S. Vinogradov, M. L. Ng, E. E. Ćavar, R. Westerström, A. Mikkelsen, E. Lundgren, and N. Mårtensson, Phys. Rev. B **75**, 245412 (2007).
[11] M. Morscher, M. Corso, T. Greber, and J. Osterwalder, Surf. Sci. **600**, 3280 (2006).
[12] M. Corso, T. Greber, and J. Osterwalder, Surf. Sci. **577**, L78 (2005).
[13] M. Corso, W. Auwärter, M. Muntwiler, A. Tamai, T. Greber, and J. Osterwalder, Science **303**, 217 (2004).
[14] A. Goriachko, Y. He, M. Knapp, H. Over, M. Corso, T. Brugger, S. Berner, J. Osterwalder, and T. Greber, Langmuir **23**, 2928 (2007).
[15] R. Laskowski, P. Blaha, T. Gallauner, and K. Schwarz, Phys. Rev. Lett. **98**, 106802 (2007).
[16] R. Laskowski and P. Blaha, J. Phys.: Condens. Matter **20**, 064207 (2008).
[17] S. Berner *et al.*, Angew. Chem., Int. Ed. **46**, 5115 (2007).
[18] M. Allan, S. Berner, M. Corso, T. Greber, and J. Osterwalder, Nanoscale Res. Lett. **2**, 94 (2007).
[19] T. Greber, L. L. Brandenberger, M. Corso, A. Tamai, and J. Osterwalder, e-J. Surf. Sci. Nanotechnol. **4**, 410 (2006).
[20] H. Dil, J. Lobo-Checa, R. Laskowski, P. Blaha, S. Berner, J. Osterwalder, and T. Greber, Science **319**, 1824 (2008).
[21] O. Bunk, M. Corso, D. Martoccia, R. Herger, P. Willmott, B. Patterson, J. Osterwalder, J. van der Veen, and T. Greber, Surf. Sci. **601**, L7 (2007).
[22] R. Widmer, S. Berner, O. Gröning, T. Brugger, J. Osterwalder, and T. Greber, Electrochem. Commun. **9**, 2484 (2007).
[23] P. Blaha, K. Schwarz, G. K. H. Madsen, D. Kvasnicka, and J. Luitz, *WIEN2k, An Augmented Plane Wave Plus Local Orbitals Program for Calculating Crystal Properties* (Vienna University of Technology, Austria, 2001).
[24] G. K. H. Madsen, P. Blaha, K. Schwarz, E. Sjöstedt, and L. Nordström, Phys. Rev. B **64**, 195134 (2001).
[25] Z. Wu and R. E. Cohen, Phys. Rev. B **73**, 235116 (2006).
[26] F. Tran, R. Laskowski, P. Blaha, and K. Schwarz, Phys. Rev. B **75**, 115131 (2007).
[27] J. P. Perdew, K. Burke, and M. Ernzerhof, Phys. Rev. Lett. **77**, 3865 (1996).
[28] W. Auwärter, M. Muntwiler, J. Osterwalder, and T. Greber, Surf. Sci. Lett. **545**, L735 (2003).
[29] A. Goriachko, Y. B. He, and H. Over, J. Phys. Chem. C **112**, 8147 (2008).
[30] A. B. Preobrajenski, M. A. Nestrov, M. L. Ng, A. S. Vinogradov, and N. Mårtensson, Chem. Phys. Lett. **446**, 119 (2007).
[31] R. F. W. Bader, *Atoms in Molecules: A Quantum Theory* (Oxford University Press, Oxford, UK, 1990).
[32] G. K. M. Madsen, P. Blaha, and K. Schwarz, J. Chem. Phys. **117**, 8030 (2002).